applied sciences

MDPI

Article

Seismic Stability of Dual Tunnels in Cohesive–Frictional Soil Subjected to Surcharge Loading

Yongge Zeng [1] and Gaoqiao Wu [2,*]

[1] Department of Civil Engineering, Shaoyang University, Shaoyang 422000, China; walker_zeng@163.com
[2] Department of Civil Engineering, Tsinghua University, Beijing 100089, China
* Correspondence: highbridgewu@gmail.com

Abstract: In this study, a self-developed adaptive finite element limit analysis (AFELA) code was adopted to explore the stability of dual tunnels in cohesive–frictional soil subjected to surcharge loading and seismic action. Parametric studies of different influential factors, including the depth of tunnels, horizontal distance between tunnels, seismic acceleration coefficient, unit weight, cohesion and internal friction angle of soils, were conducted using the AFELA code. An adaptive meshing technique was adopted for optimal accuracy and efficiency, and a pseudostatic method was used to simulate the seismic action. Strict upper bound (UB) and lower bound (LB) results with relative errors of less than 7% were acquired. Detailed design tables were presented to facilitate the engineering design, and three typical failure patterns, including single side-wall failure, half-cross-shaped failure and cross-shaped failure, corresponding to different stable levels, were summarized for a deeper insight into how the failure mechanism evolved under different conditions. The results indicated that the variations in soil unit weight and void depth affected the seismic bearing capacity almost linearly. Furthermore, the dual tunnel system is vulnerable to seismic actions, and the stability of tunnels was further undermined by the adverse effects of additional seismic-caused interactions between two adjacent tunnels.

Keywords: seismic bearing capacity; adaptive finite element limit analysis; tunnel stability; dual tunnels

check for updates

Citation: Zeng, Y.; Wu, G. Seismic Stability of Dual Tunnels in Cohesive–Frictional Soil Subjected to Surcharge Loading. *Appl. Sci.* **2022**, *12*, 2779. https://doi.org/10.3390/app12062779

Academic Editors: Daniel Dias and Edyta Plebankiewicz

Received: 2 September 2021
Accepted: 7 March 2022
Published: 8 March 2022

Publisher's Note: MDPI stays neutral with regard to jurisdictional claims in published maps and institutional affiliations.

Copyright: © 2022 by the authors. Licensee MDPI, Basel, Switzerland. This article is an open access article distributed under the terms and conditions of the Creative Commons Attribution (CC BY) license (https://creativecommons.org/licenses/by/4.0/).

1. Introduction

With the rapid development of urbanization and highway engineering, it is difficult for road construction to avoid encountering hills, especially in the mountainous areas. A detour may lead to creating an unnecessary distance of road and causing an extensive amount of work. In view of this, the tunnel is considered a reasonable construction type to cope with such circumstances.

The single tunnel, as the basic tunnel type, was investigated by theoretical methods [1–5] and numerical methods [6–16]. However, dual parallel tunnels are more economical than the single tunnels, and the stability analysis of dual tunnels is relevant. Soliman et al. [17] employed a finite element limit analysis (FELA) to investigate the bearing capacity of double-tube tunnels. The results indicate that the solution of a single tunnel can be adopted to find double-tube solutions. Kim et al. [18] experimentally explored the effects of several factors on the bearing capacity of double tunnels. Lanzano et al. [19] and Abate et al. [20] conducted centrifuge experiments to investigate the stability of tunnels in sand and soil, respectively. Osman [21] adopted an upper bound limit analysis to investigate the undrained stability of twin tunnels, the variation of shear strength was taken into account. Using upper bound FELA, Sahoo and Kumar [22] presented a series of sensitivity analyses for an insight into the bearing capacity of double tunnels in c-φ soil. Then, they analyzed the lining pressure of dual tunnels in pure cohesion soil and c-φ soil, respectively [23]. By combining a FELA and rigid block mechanism, the bearing capacity of circular and square tunnels was investigated by Yamamoto et al. [24] for c-φ soil and Wilson et al. for undrained

soil. Detailed design charts were offered for engineering use. Recently, Zhang et al. [25,26] and Yang et al. [27,28] used the upper bound finite element method to propose sensitivity analyses of double tunnels with different shapes, including pure circular, horseshoe and elliptical tunnels. Additionally, adaptive finite element limit analysis (AFELA) was used by Xiao et al. [29] to investigate the stability of double tunnels in c-φ soil at different depths; then, the cases of tunnels in rock mass were considered. In recent years, owing to the frequent earthquakes around the world (e.g., EI Centro, Wenchuan, Loma Prieta, Ancona and Fukushima earthquakes, etc.), the seismic stability issue of tunnels became a hot topic. Vahid and Alireza [30] used incremental nonlinear dynamic analysis to evaluate the seismic reliability of RC tunnel-form structures. Then, Vahid et al. [31] developed a new method to assess the seismic reliability of RC tunnel-form structures by a combined systems approach. To investigate the seismic responses and damage mechanisms of tunnels, Yue et al. [32] conducted a series of shaking table model tests. The test results offered deep insights into the seismic performance of tunnels with relatively shallower depths. Considering the advantages of numerical simulations, many researchers chose to investigate this problem numerically. Maleska et al. [33] adopted finite element analysis code DIANA to explore how RC soil–steel composite tunnels behave under seismic action. Sahoo and Kumar [7,16] and Chakraborty and Kumar [12] combined the FELA and the pseudo-static method to investigate the seismic stability of a single tunnel under various conditions. Their investigations were verified with results from other methods, demonstrating that the FELA can effectively solve seismic stability issues.

However, aside from these aforementioned contributions, there is no information regarding the seismic stability of dual tunnels in c-φ soil. As mentioned above, more dual parallel tunnels systems would be constructed on account of its advantages; therefore, investigating the seismic stability of dual parallel tunnels system is necessary. In view of this, a self-developed AFELA code is adopted to assess the seismic bearing capacity of dual circular tunnels in c-φ soil. The sensitivity analyses of a series of influential factors, including the distance between the dual tunnels, depth of the tunnels, cohesion, internal friction angle, unit weight of the soil and seismic acceleration factor, are presented. The variation trends of critical interaction distance between tunnels are revealed. Through an analysis of different failure mechanisms, three typical failure patterns are summarized, and the scope of collapse is discussed in depth. Furthermore, design tables with detailed results from AFELA are offered for engineers to utilize.

2. Problem Definition

Figure 1 presents the main influential factors of a dual tunnels system. Following previous studies [6–9,12,15,16,22–26,29], tunnel length is considered as infinite; therefore, the plain strain model is suitable for this issue. The size of this numerical model is 60D in width and 30D in depth, which is big enough to avoid the boundary effect. The diameter of the tunnels is D. The dimensionless horizontal distance between the tunnels is S/D. The dimensionless cover depth of the voids is H/D. The continuous distributed load σ_s is applied to the surface of the soil domain. This study assumes the soil to be isotropic and homogeneous. Additionally, the soil obeys the Mohr–Coulomb yield criterion and associated flow rule with cohesion c, internal friction angle φ and unit weight γ. Following previous studies [29], the above parameters have the following values: φ = 5°, 10°, 15°, 20°; $\gamma D/c$ = 0 and 1. The numerical model is a rigid half space, and the top surface is free. Additionally, seismic action is simulated by pseudostatic method, i.e., applying an earthquake acceleration factor k_h to the soil domain [7,16]. Additionally, the cases of k_h = 0, 0.05, 0.1, 0.15 and 0.2 are considered in this study. For a more convenient expression of the seismic bearing capacity, a stability factor $Ncs = \sigma_s/c$ [34] is introduced, which can be expressed as follows:

$$N_{cs} = \frac{\sigma_s}{c} = f\left(\frac{H}{D}, \frac{S}{D}, \frac{\gamma D}{c}, \phi, k_h\right) \quad (1)$$

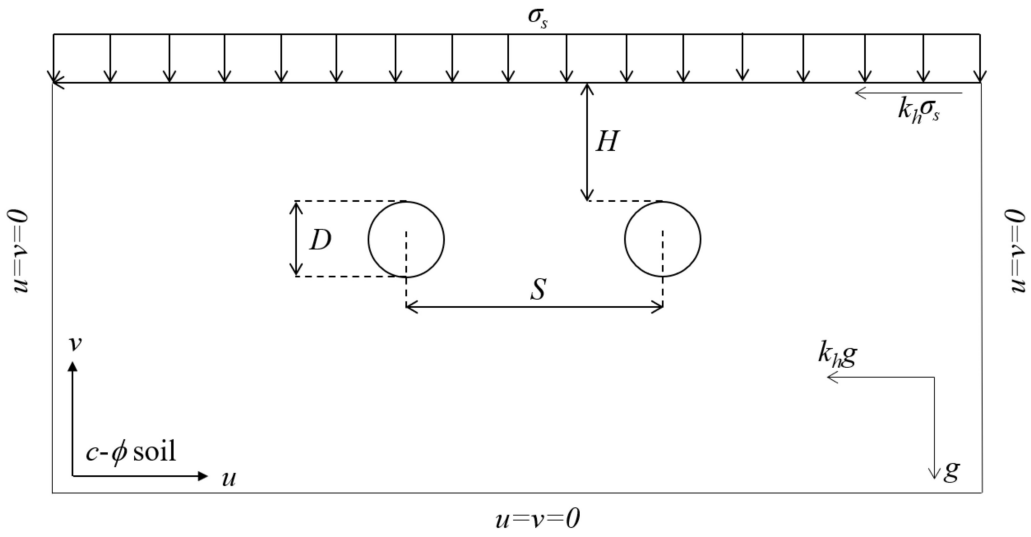


Figure 1. Problem definition.

3. AFELA Model

As an advanced method, FELA has been widely used in engineering practices [6–16]. The FELA can assess accurate ultimate loads by a combination of the limit theorems of plasticity and finite elements [35]. Strictly close lower bound (LB) results and upper bound (UB) results can be obtained by a reasonable construction of statically admissible stress field and kinematically admissible velocity field, respectively. Additionally, the true ultimate bearing capacity is located between the LB and UB results. To achieve precise results, a discontinuous finite element formulation is introduced into the present study for discrete UB [36] and LB [37] issues. The use of the discontinuous finite element formulation in the static form of limit analysis leads to two nonlinear optimization models, which can be presented as the same form [38,39]:

$$\textbf{Minimize} \qquad \lambda \tag{2}$$

$$\textbf{Subject to} \qquad \sigma = p_0 + \lambda p \tag{3}$$

$$f(\sigma_j) \le 0, j = 1, \ldots, n_\sigma \tag{4}$$

where λ is the load multiplier, B^{T} is the operator of discrete equilibrium type, $\sigma = (\sigma_1, \ldots, \sigma_{n_\sigma})^{\mathrm{T}}$ is the vector of σ_j, n_σ is the sum of discrete stresses, p_0 and p are the vectors of multiplier force and prescribed force, and f is the yield function.

The authors developed a nonlinear optimization algorithm to solve Equations (2)–(4). This algorithm is an improved version of the feasible arc interior point algorithm (FAIPA) [40]. To reach a precise result, a self-developed adaptive remeshing technique [41] is employed in the AFELA code. This technique is developed on the basis of bounds gap error estimator, which can decompose the overall bounds gap, discrepancy of the UB and LB calculated with identical meshes into positive contributions from all elements in the mesh [38,39]. This adaptive meshing strategy is composed of adjusting element sizes in the field to equably distribute local errors (measured by elemental bound gaps) to each element of this mesh. Through the use of the adaptive meshing program, more accurate results can be obtained. More detailed information about the self-developed adaptive meshing technique proposed is presented as follows:

$$d_n(\mathbf{x}) = \beta(\mathbf{x}) \cdot d_o(\mathbf{x}), \mathbf{x} \in \Omega \tag{5}$$

$$\text{s.t.} \underline{\beta} \le \beta(\mathbf{x}) = \frac{\sqrt{4\Delta / \left(\sqrt{3} Nel \cdot \rho(\mathbf{x})\right)}}{d_o(\mathbf{x})} \le \overline{\beta} \tag{6}$$

where *Nel* is the element number of the optimized mesh; d_o is the distribution of element sizes of original mesh; d_n is the distributions of element sizes for the optimized mesh; $\beta(\mathbf{x})$ is the distribution for the decreasing or increasing rate of element sizes in the optimized mesh subject to the upper and lower limits of $\overline{\beta}$ and β; $\rho(\mathbf{x})$ is the distribution for the intensity of the dissipation gap; and Δ is the overall dissipation gap, which can be decomposed into elemental contributions Δ^e from all the elements in the entire mesh [35]:

$$\Delta = \sum_{elements} \Delta^e = \lambda^{\mathrm{UB}} - \lambda^{\mathrm{LB}} \tag{7}$$

where Δ^e is the elemental dissipation gap and λ^{UB} and λ^{LB} are the UB and LB results of ultimate load multipliers, respectively. As space is limited, a further description will not be introduced here. Detailed information regarding the code can be seen in Zhang's work [41].

Figure 2 presents a detailed mesh arrangement for dual tunnels in cohesion–frictional soil by the self-developed code mentioned above. This study adopts four refinement steps to reach the high precision of computation. The initial and final number of elements is set as 2000 and 8000 to guarantee accuracy and efficiency. By dint of the remeshing technique, the mesh would be performed automatically following the preset element number and iteration number; therefore, it can be seen that the mesh around the tunnel is denser than other areas. The soil is governed by the Mohr–Coulomb criterion, and the whole field of soil is large enough (60D in width and 30D in depth) to avoid the boundary effect. In addition, the relative errors between UB and LB results are less than 7% for all cases in this study.

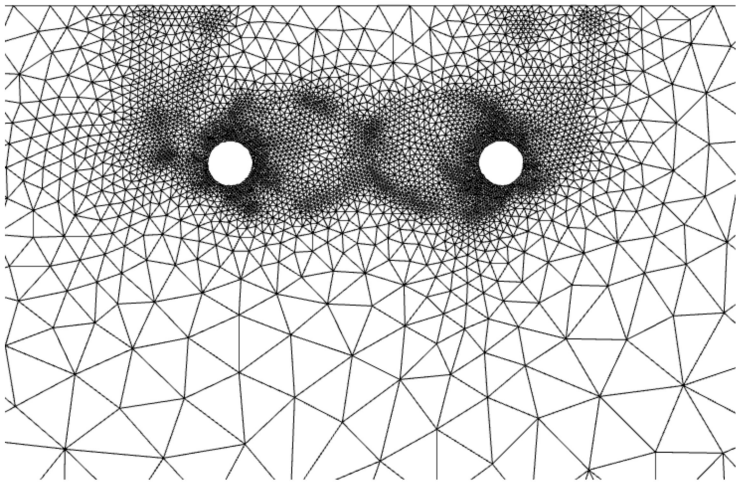


Figure 2. Detailed mesh arrangement in AFELA.

4. Results and Discussions

The cases of double tunnels in c-φ soil without seismic action and single tunnels in c-φ soil with seismic action were compared with the previous literature [16,28] and Optum G2 (a commercial FELA software) [42] to verify the reliability of the present model. It should be noted that the N_{cs} in Figure 3 represents the bearing capacity factor. A specific definition can be seen in the corresponding literature [16,28]. It can be seen from Figure 3 that, for all cases, the magnitude and variation trends of UB and LB AFELA results are close to other results. Additionally, slight errors are caused by the different meshing strategy. The maximum error of LB and UB AFELA results occurs in Figure 3 with the $\gamma D/c$ = 0 and S/D = 8. The UB and LB results are 7.735 and 7.22, respectively, and the greatest error is 6.89%, which is calculated by Equation (8):

$$\text{Error} = \left| \frac{2(\mathrm{UB} - \mathrm{LB})}{\mathrm{UB} + \mathrm{LB}} \right| \cdot 100\% \tag{8}$$

The slight error means that this AFELA model is reliable. Additionally, to further reduce errors, this study uses the mean value of UB and LB AFELA results to assess the seismic bearing capacity.

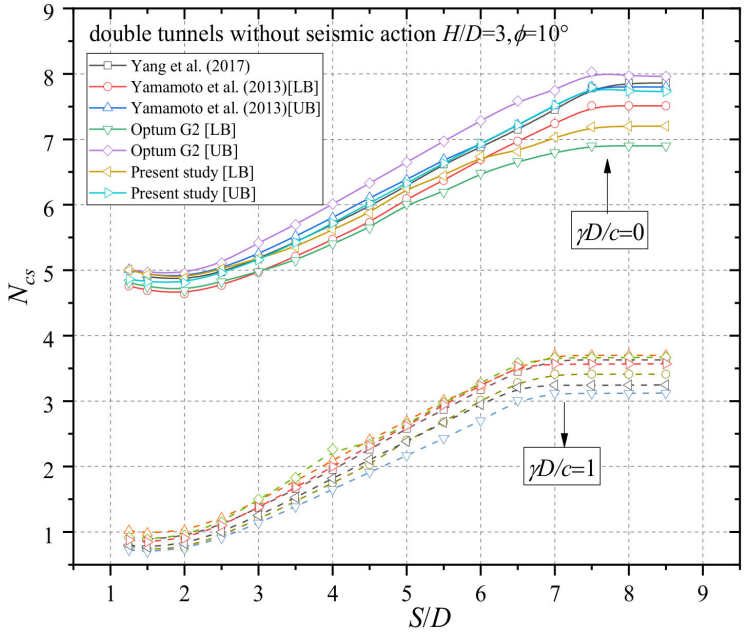


Figure 3. Comparison of N_{cs}-S/D curves with different $\gamma D/c$ for double tunnels without seismic action.

Figure 4 shows the effect of $\gamma D/c$ on the seismic bearing capacity factor with different S/D, H/D and φ. As expected, the seismic bearing capacity decreases with the increase in $\gamma D/c$. This is because the heavier soil mass would apply a greater load on the tunnels, and less cohesion means a decrease in soil strength. Furthermore, it can be seen that the curves of each case are nearly straight. This means that the $\gamma D/c$ linearly affects the seismic bearing capacity. In view of this, $\gamma D/c = 0$ and $\gamma D/c = 1$ are adopted in subsequent investigations for simplicity. The seismic bearing capacity with any value of $\gamma D/c$ can be predicted from two known results of $\gamma D/c = 0$ and $\gamma D/c = 1$.

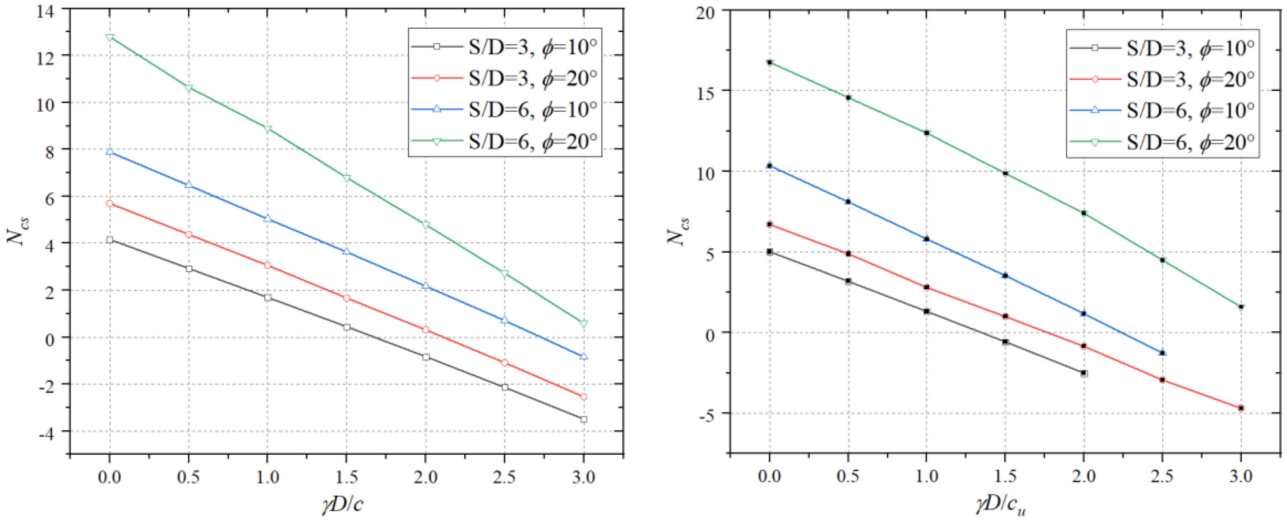
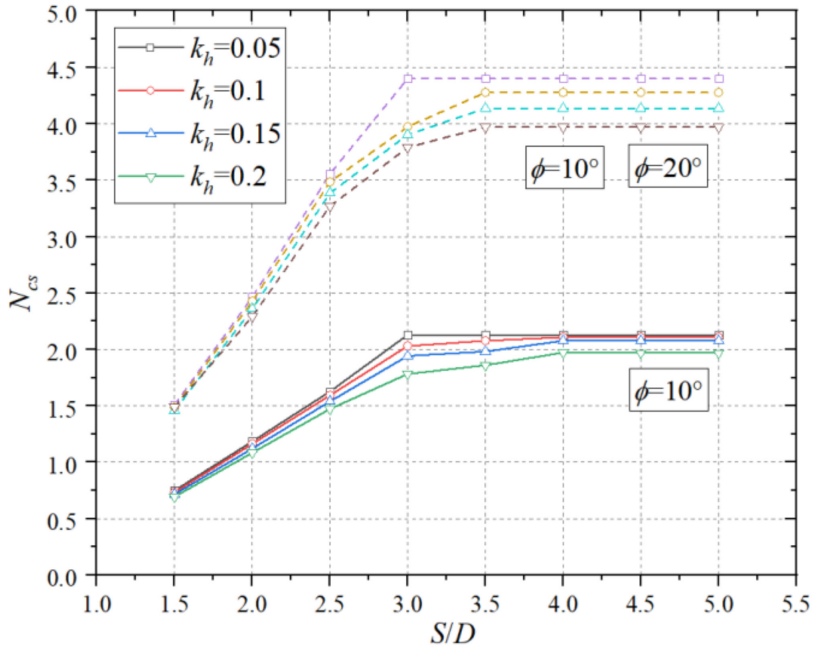


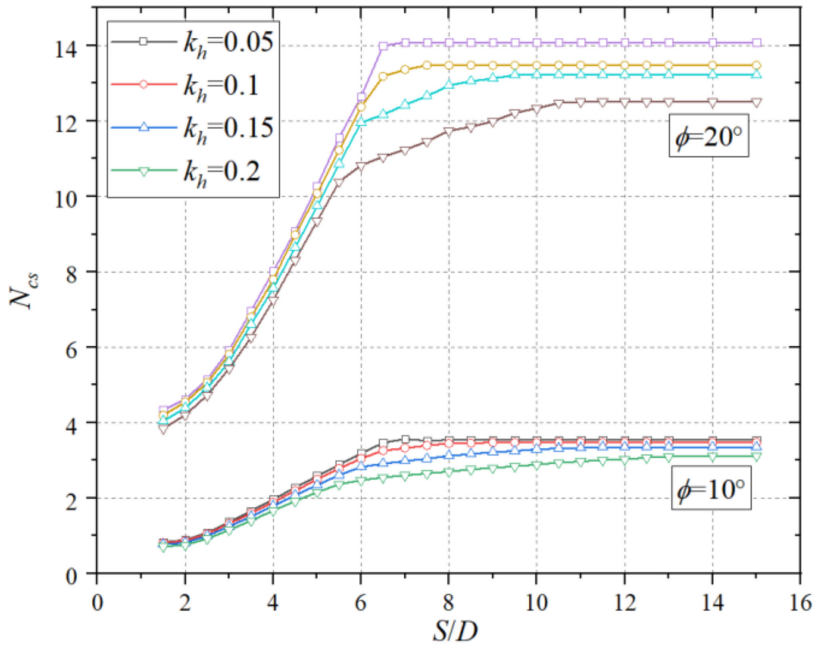
Figure 4. N_{cs}-$\gamma D/c$ curves with $k_h = 0.1$ and different S/D and φ for (**a**) $H/D = 2$; and (**b**) $H/D = 3$.

The interaction of tunnels significantly affects their stability. The estimation of critical interaction distance is the essential question in engineering practice. Figure 5 shows the effect of horizontal distance between tunnels with different influential factors. It can be determined that, for all cases, the seismic bearing capacity increases with the increase in S/D until the N_{cs} reaches an extremum value. This is because the further the distance between dual tunnels is, the weaker the interaction between the tunnels becomes. Additionally, the extremum value is the critical interaction distance mentioned above, beyond which the dual tunnels would not impact each other. It can be observed that the critical interaction distance of cases with a greater seismic coefficient k_h is greater. This demonstrates that the seismic action would intensify the interaction between dual tunnels. Additionally, the stronger the seismic action is, the greater the interaction becomes. Through comparisons between Figure 5a,b, it can be observed that the seismic bearing capacity of cases with a deeper tunnel depth is greater than those cases with a shallower tunnel depth. Furthermore, the critical interaction distance of H/D = 1 ranges from 3 to 4, whereas the critical interaction distance of H/D = 3 ranges from 7 to 14. Namely, the deeper the tunnels are located, the greater the critical interaction distance of the tunnels becomes. It can be seen that the seismic bearing capacities of Figure 5c are greater than those of Figure 5a, which corresponds to Figure 4. Regarding the effect of φ on the critical interaction distance, it can be observed that, in cases of small seismic action (k_h = 0.05, 0.1), the critical distance of different φ is almost maintained as equal, whereas if the seismic action becomes larger (k_h = 0.15, 0.2), the critical interaction distance between tunnels would increase with a decreasing φ. In Figure 5b, for instance, the critical distance with k_h = 0.1 is 7.5 for φ = 10° and 20°. As for cases of k_h = 0.2, the critical distance with φ = 10° is 14, while the critical distance with φ = 20° is 11. Moreover, the increase in φ would lead to a greater bearing capacity, and the greater the value of φ is, the steeper the gradient of variation curve becomes. Furthermore, it can be seen from Figure 5 that the curves of φ = 10° locate closer than the curves of φ = 20°, which means that seismic action exerts less effect on cases of smaller internal friction angles.

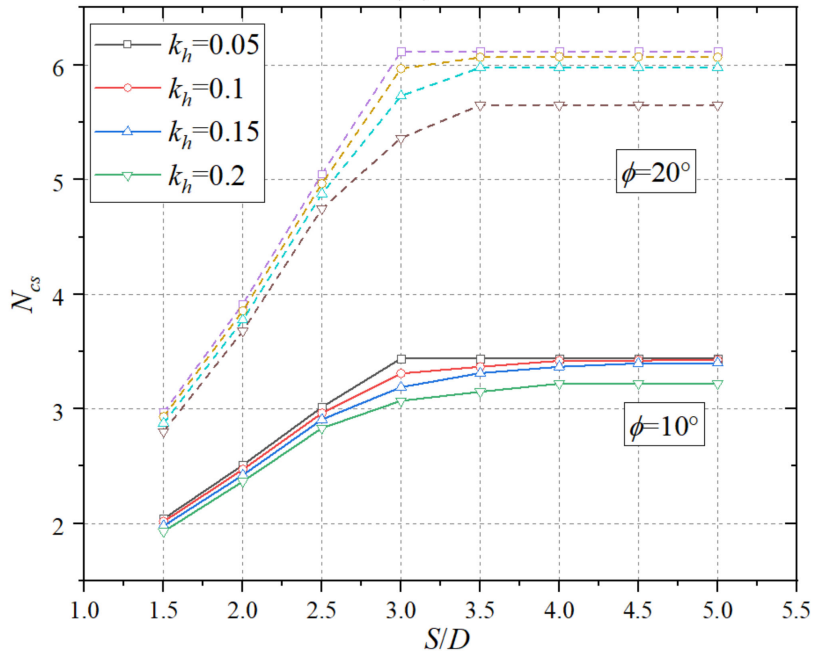


(**a**)

Figure 5. *Cont.*



(**b**)



(**c**)

Figure 5. N_{cs}-S/D curves with different k_h and φ for (**a**) $\gamma D/c = 1$, $H/D = 1$; (**b**) $\gamma D/c = 1$, $H/D = 3$; and (**c**) $\gamma D/c = 0$, $H/D = 1$.

To present a deeper and more visualized insight of the critical distance, Figure 6 depicts the variation of N_{cs} with different internal friction angle. It can be seen that for all subfigures, the critical distance decreases with the increase in φ. Through comparisons between Figure 6a,b, it can be seen that the critical distance would decrease with the increase in $\gamma D/c$. Additionally, by contrasting the data of Figure 6b,c, it is clear that the deeper the tunnel depth is, the greater the critical distance becomes. The critical distance of tunnels would also increase with a stronger seismic action. This trend is revealed through comparisons of Figure 6c,d.

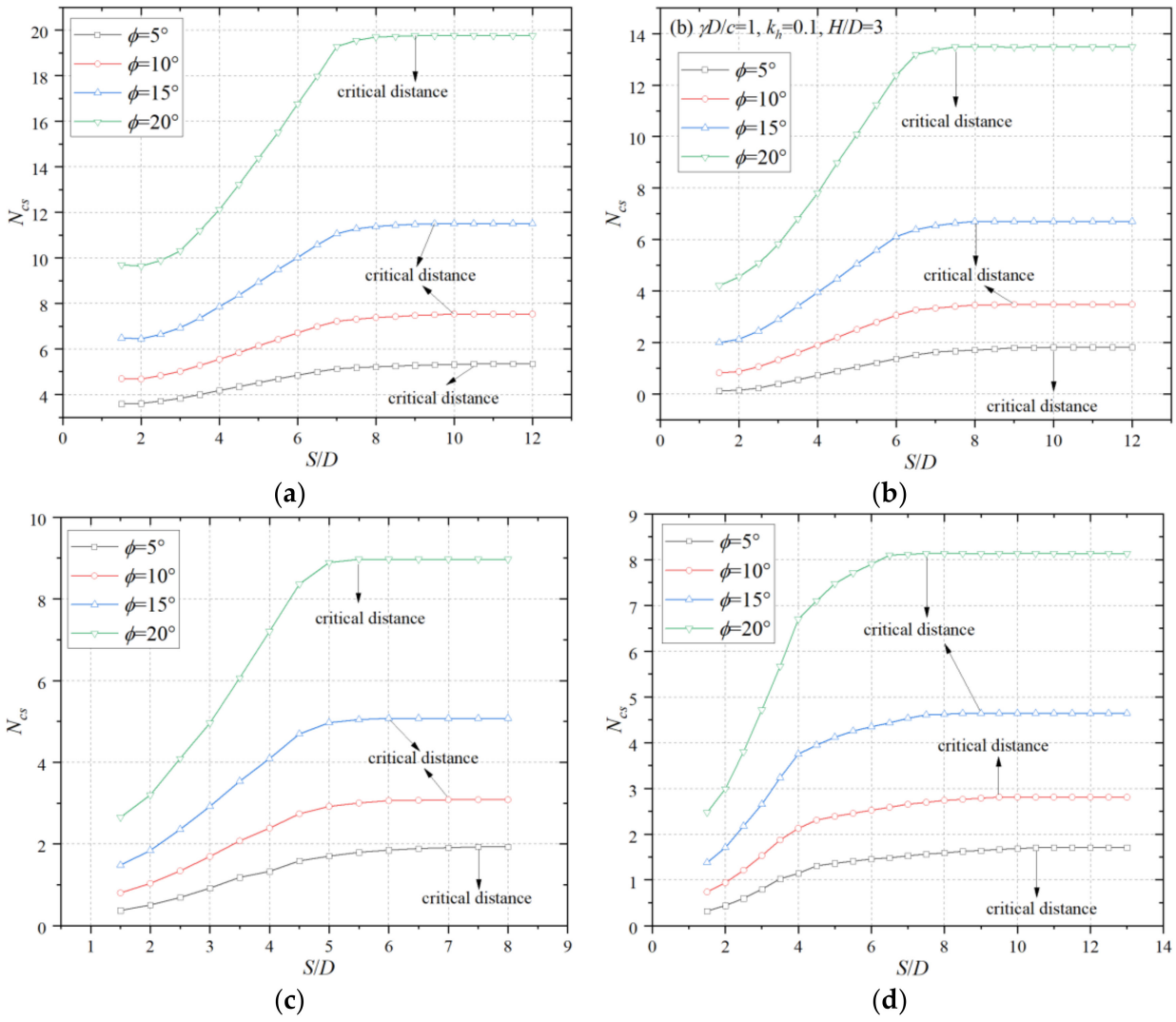


Figure 6. N_{cs}-S/D curves with different φ for (**a**) $\gamma D/c = 0$, $k_h = 0.1$, $H/D = 3$; (**b**) $\gamma D/c = 1$, $k_h = 0.1$, $H/D = 3$; (**c**) $\gamma D/c = 1$, $k_h = 0.1$, $H/D = 2$; and (**d**) $\gamma D/c = 1$, $k_h = 0.2$, $H/D = 2$.

Figure 7 depicts the variation of seismic bearing capacity with different internal friction angle φ. As expected, all curves of Figure 7 show an uptrend, which means the bearing capacity increases with the increase in φ. Additionally, for all figures, the gradient of the curves becomes steeper with the deeper depth of tunnels. This indicates that, for cases with a deeper depth of tunnels, the internal friction angle would have a more significant influence on seismic bearing capacity. Furthermore, it can be seen from Figure 7a–c that, when $\gamma D/c = 0$, the difference values of N_{cs} between different H/D tend to be greater with the increase in φ, while the difference values become smaller with the increase in φ with $\gamma D/c = 2$. This phenomenon indicates that, for cases of small $\gamma D/c$ (Figure 7a), the depth of tunnels has a greater effect on the seismic bearing capacity with a greater φ, whereas for cases of high $\gamma D/c$ (Figure 7c), the effect of the tunnel depths on the seismic bearing capacity attenuates with the increase in φ. Additionally, this trend of $\gamma D/c = 1$ is in between cases of $\gamma D/c = 0$ and $\gamma D/c = 2$. The H/D has almost no effect on seismic bearing capacity at the overlapped part in Figure 7b. Through comparisons between Figure 7b,d, it is clear that the seismic bearing capacity of cases with $S/D = 5$ is greater than cases with $S/D = 3$. Additionally, the variations in the internal friction angle would incur a greater influence on seismic bearing capacity with a further distance between tunnels. This tendency is more distinct with the deeper depth of tunnels.

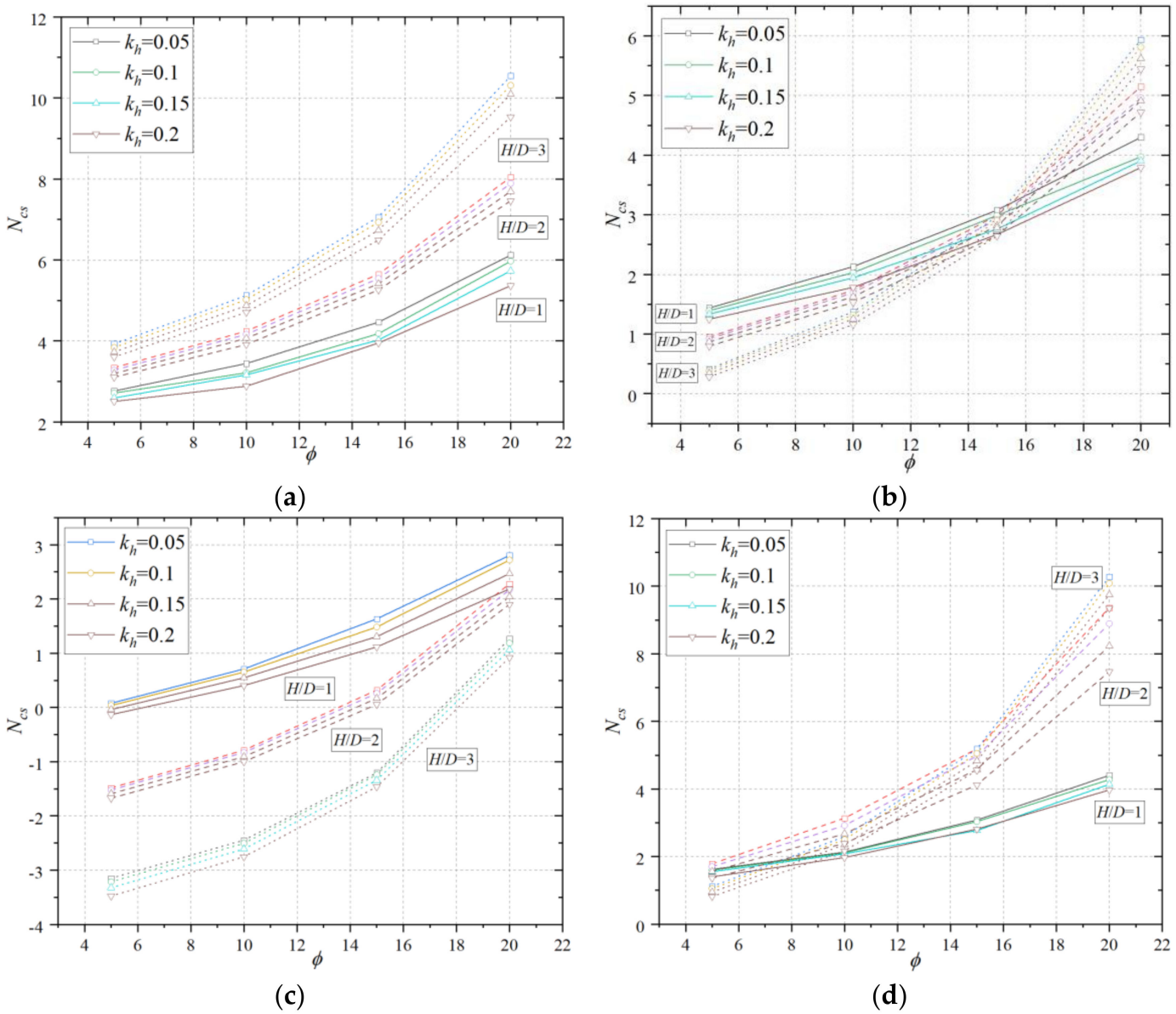


Figure 7. N_{cs}-φ curves with different H/D and k_h for (**a**) $\gamma D/c = 0$, $S/D = 3$; (**b**) $\gamma D/c = 1$, $S/D = 3$; (**c**) $\gamma D/c = 1$, $S/D = 1.5$; and (**d**) $\gamma D/c = 1$, $S/D = 5$.

Figure 8 depicts the variation trend of seismic bearing capacity with different depths of the tunnels. It can be seen that, for all cases, the curves are straight, which means the H/D would have a linear impact on N_{cs}. Additionally, the gradients of curves with different k_h are almost the same. This indicates that seismic action affects the seismic bearing capacity almost proportionally. In addition, for cases of $\gamma D/c = 0$, the values of N_{cs} increase repeatedly with the apparent increase in H/D. Additionally, a trend can be observed from the curve gradients that the variation in H/D has a strong influence on the N_{cs} for cases of greater internal friction angles. By contrast, in Figure 8b, the seismic bearing capacity increases with the increase in the tunnel depth for large φ, while for cases of small internal friction angle ($\varphi \leq 15°$), the seismic bearing capacity decreases with an increasing H/D.

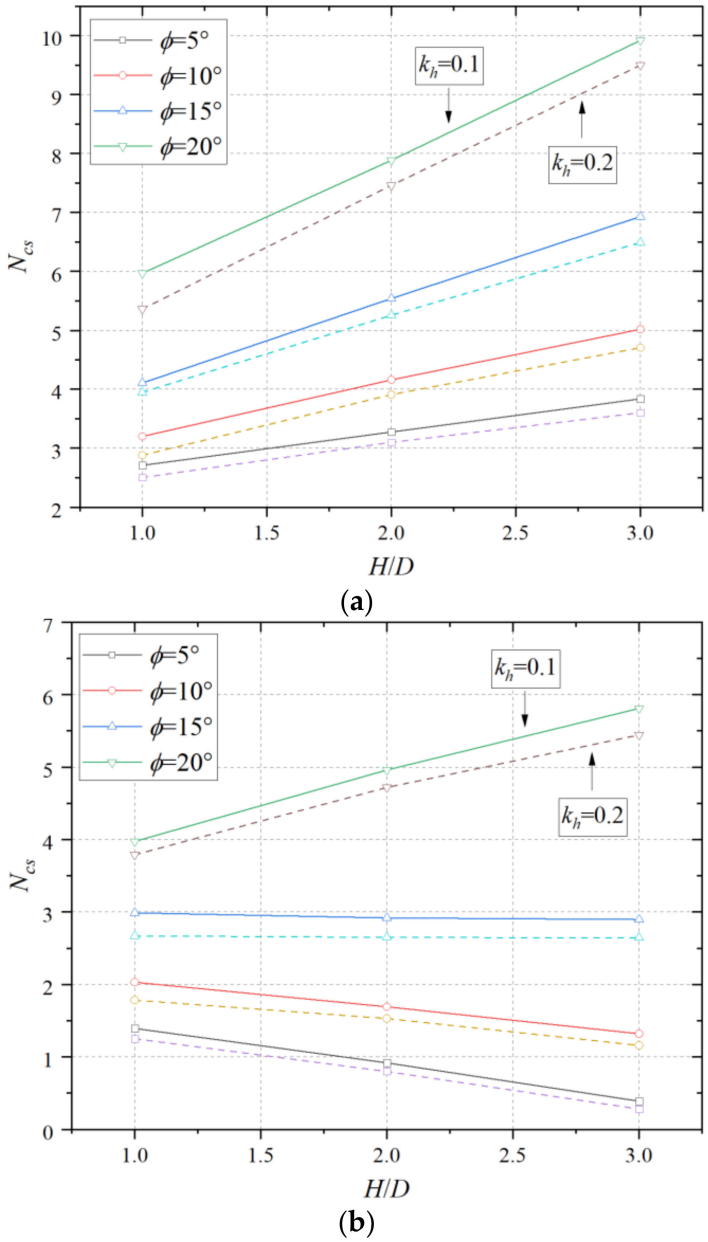


Figure 8. N_{cs}-H/D curves with different φ and k_h for (**a**) $\gamma D/c$ = 0, S/D = 3; and (**b**) $\gamma D/c$ = 1, S/D = 3.

5. Failure Mechanisms

The scope of the collapse and the failure patterns of the double tunnels are the key issues in engineering practice. Figures 9–12 present the distribution of shear dissipation for a better understanding of how the failure patterns evolved with different conditions.

Figure 9 shows the failure mechanisms of k_h =0.1, H/D = 3, $\gamma D/c$ = 1 and φ = 10° with different S/D. Three typical failure patterns of the double tunnels are revealed: (1) cross-shaped failure, which is depicted in Figure 9a,b; (2) half-cross-shaped failure, which is depicted in Figure 9c; and (3) single side-wall failure, which is depicted in Figure 9d. It can be seen from Figure 9a,b that, when the tunnels locate close to each other, the majority of failure curves are at the pillar between the tunnels, and then the collapse extends from the tunnels to the ground surface. The cross-shaped failure zone, which comprises of two wedges indicates that the interaction of tunnels is dominant, and this strong interaction can significantly reduce seismic bearing capacity. With the increase in S/D (depicted in Figure 9c), one failure curve of crossed failure zone rotates clockwise, and there is only

one failure curve between the double tunnels. This half-cross-shaped failure means that the interaction between the double tunnels becomes weaker with the increase in S/D. Additionally, when $S/D = 9$, only two failure curves extend to the surface ground from the side-wall of a single tunnel. Namely, double tunnels have no influence on each other. Furthermore, it can be observed that the scope of influence on the ground surface broadens with a greater S/D until the failure pattern becomes a single side-wall failure.

Figure 10 shows the effect of the tunnel depth on the failure mechanisms. Clearly, the failure patterns shift to the cross-shaped failure from a single side-wall failure with the increase in tunnel depth. In view of this, it can be speculated that the deeper the tunnel depth is, the stronger the interaction between the double tunnels is. Additionally, the scope of influence clearly becomes wider with the deeper depth of the tunnels.

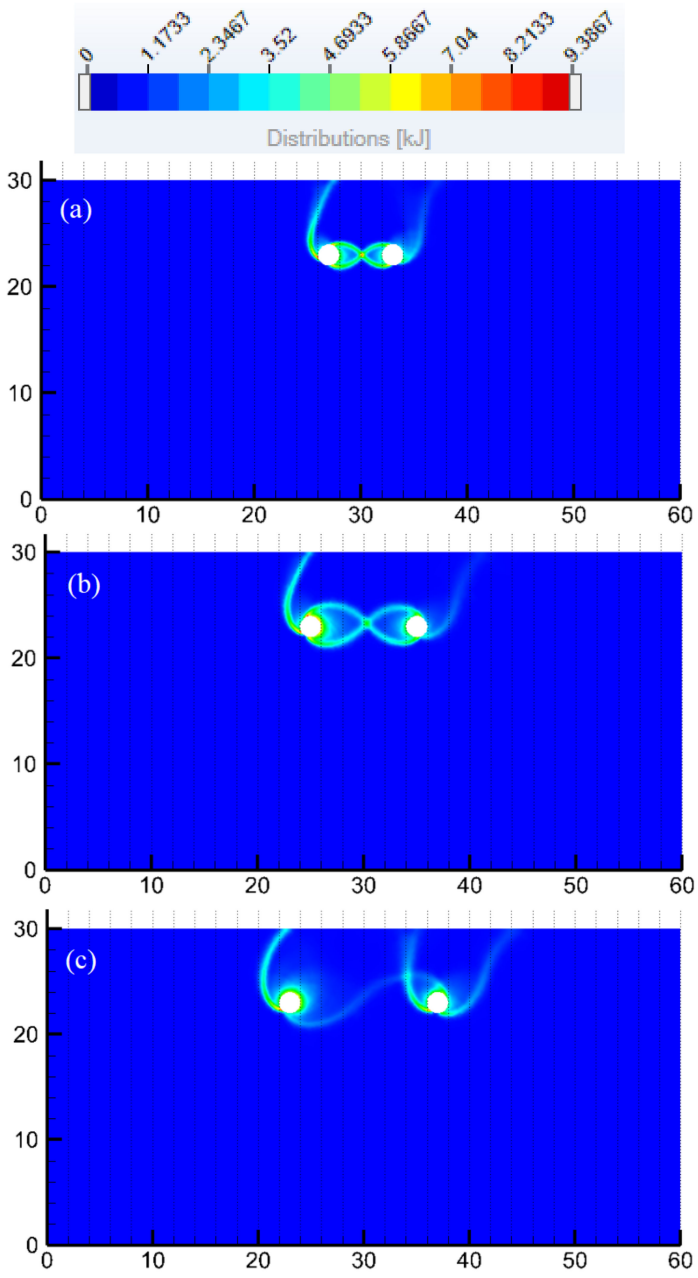


Figure 9. *Cont.*

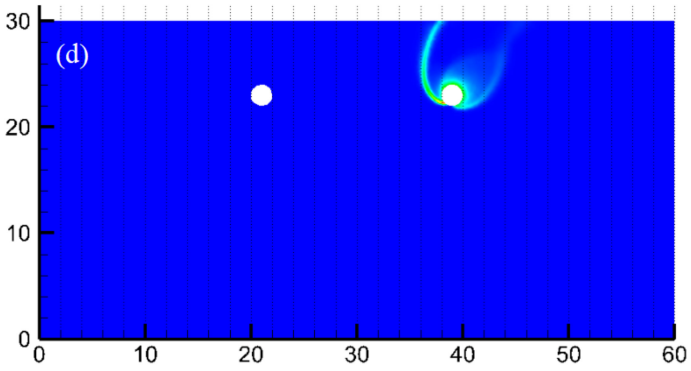


Figure 9. Upper bound failure mechanisms with H/D = 3, $\gamma D/c$ = 1, k_h = 0.1 and φ = 10° for (**a**) S/D = 3; (**b**) S/D = 5; (**c**) S/D = 7; and (**d**) S/D = 9.

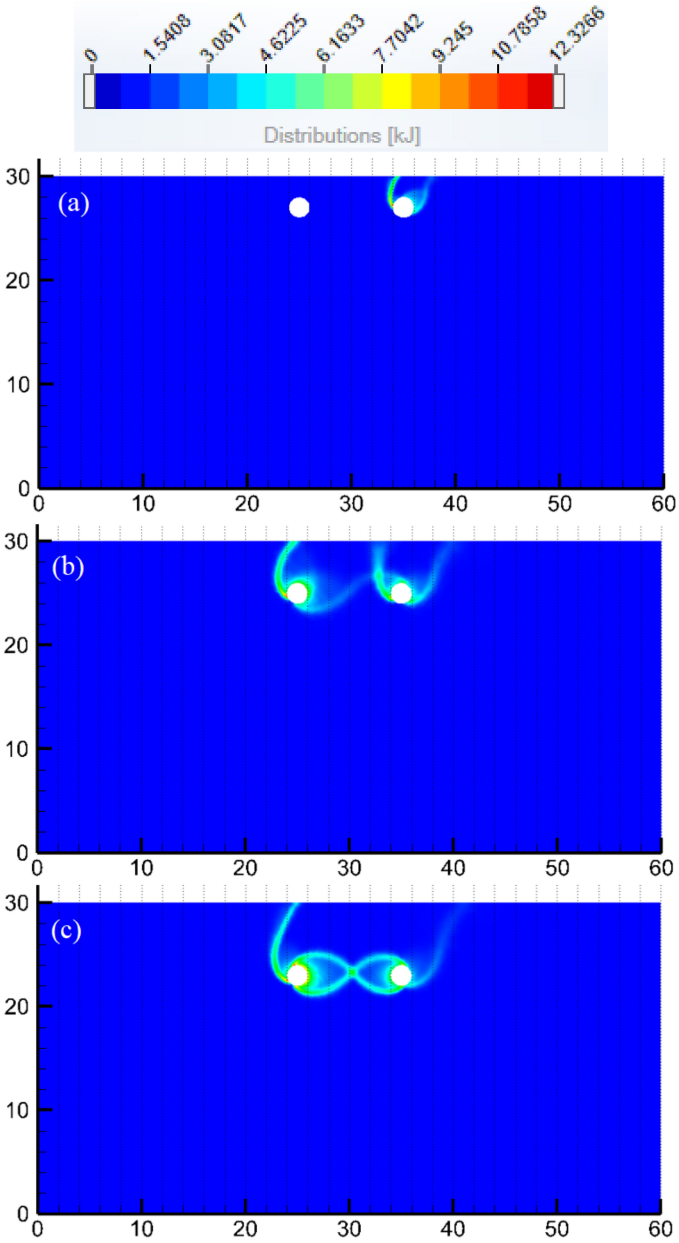


Figure 10. Upper bound failure mechanisms with S/D = 3, $\gamma D/c$ = 1, k_h = 0.1 and φ = 10° for (**a**) H/D = 1; (**b**) H/D = 2; and (**c**) H/D = 3.

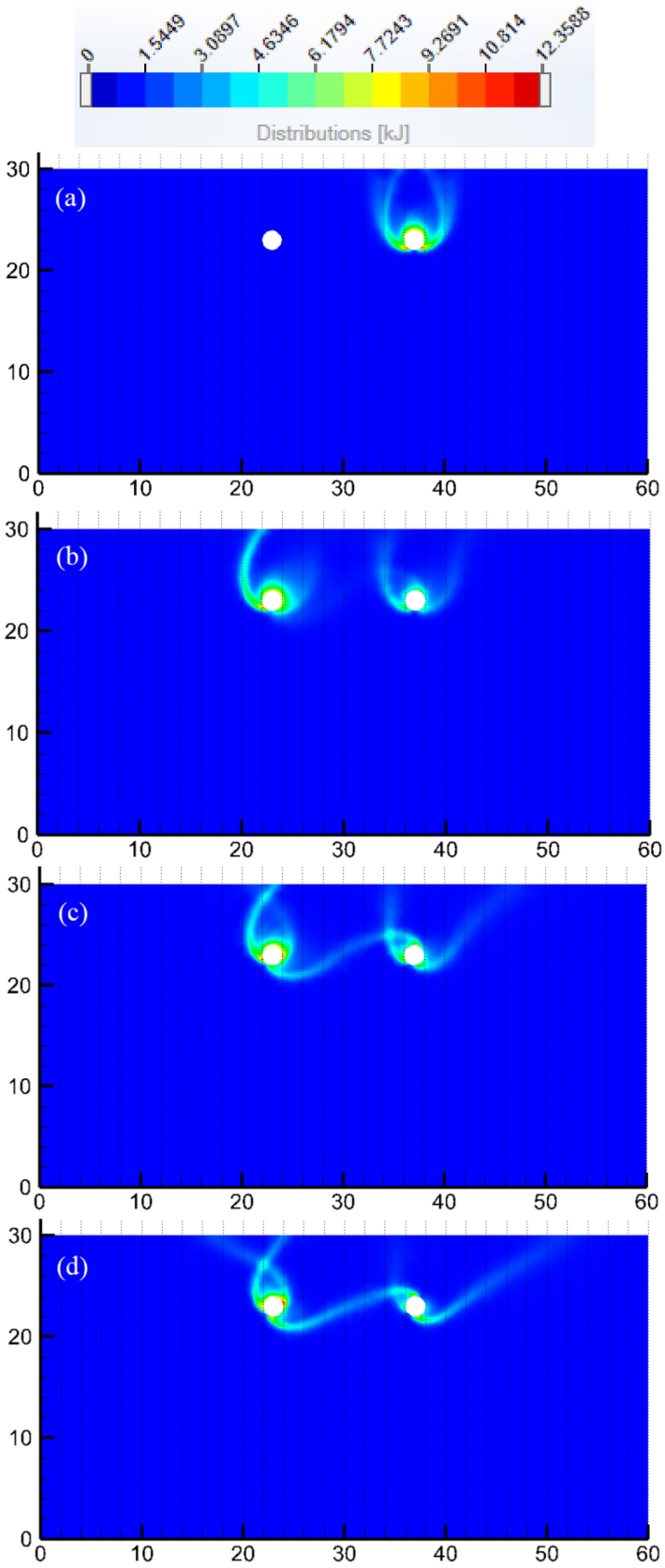


Figure 11. Upper bound failure mechanisms with $S/D = 7$, $H/D = 3$, $\gamma D/c = 1$, and $\varphi = 10^{\circ}$ for (**a**) $k_h = 0$; (**b**) $k_h = 0.1$; (**c**) $k_h = 0.2$; and (**d**) $k_h = 0.3$.

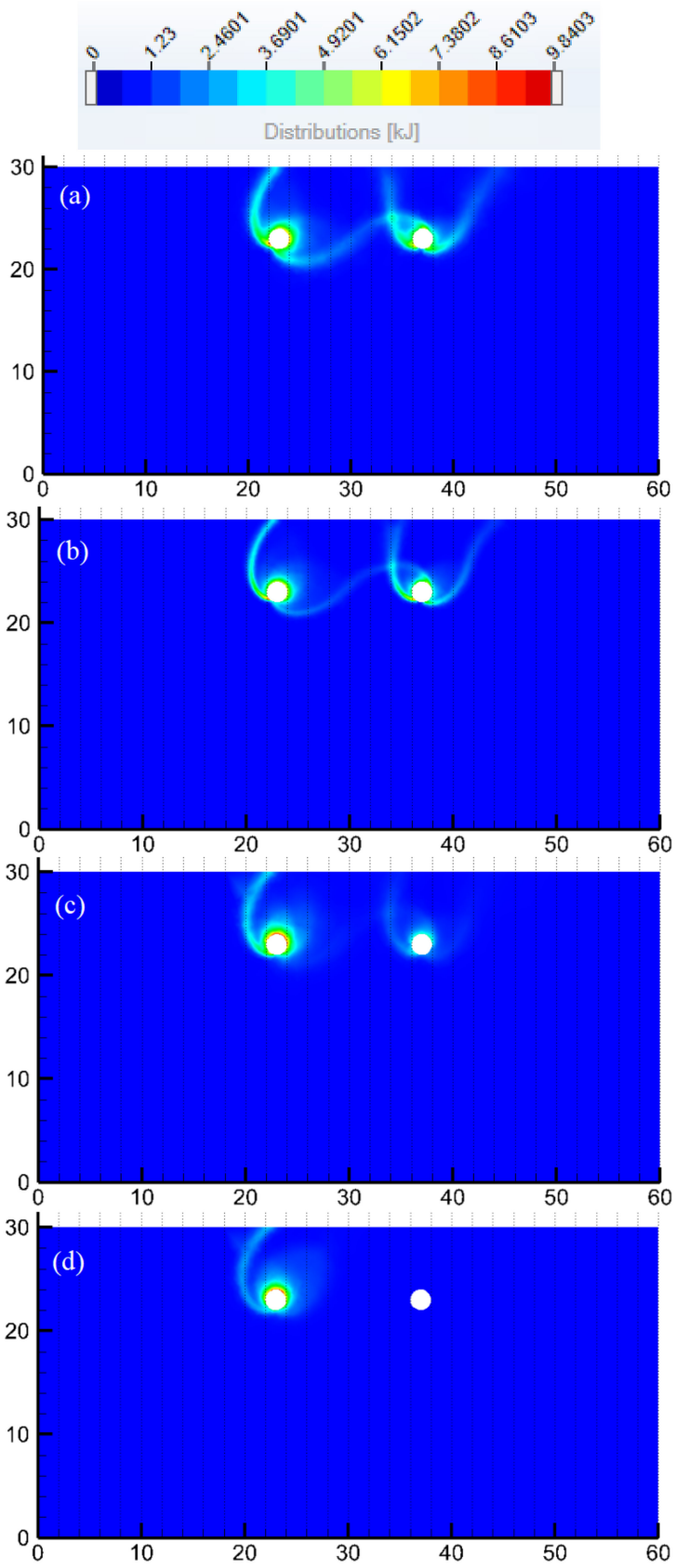


Figure 12. Upper bound failure mechanisms with $S/D = 7$, $H/D = 3$, $\gamma D/c = 1$ and $k_h = 0.1$ for (**a**) $\varphi = 5°$; (**b**) $\varphi = 10°$; (**c**) $\varphi = 15°$; and (**d**) $\varphi = 20°$.

Figure 11 shows the failure patterns of $S/D = 7$, $H/D = 3$, $\gamma D/c = 1$ and $\varphi = 10°$ with different seismic factor k_h. Figure 11a shows a single side-wall failure. It can be seen from Figure 11b–d that the failure patterns change to the half-cross-shaped failure. Additionally, the connection curve between the double tunnels becomes more distinct with a greater seismic factor. This phenomenon indicates that the interaction of the tunnels would be stronger with the increase in k_h. Based on this observation, it can be predicted that, for cases with multi tunnels/voids, the system is vulnerable to seismic actions, and its seismic bearing capacity would be further undermined by the side effect of additional interactions between vulnerable joints (e.g., underlying tunnels/caves). Furthermore, through the comparisons of Figure 11a–d, it can be observed that the failure curves tend to rotate clockwise with the increase in k_h. This rotation phenomenon would broaden the failure curves on the surface ground, illustrating that stronger earthquakes can broaden the sphere of collapse.

Figure 12 presents the effect of the internal friction angle on the failure mechanism. The failure patterns of Figure 12a,b are half-cross-shaped failures, and the spheres of collapse are nearly the same. Furthermore, it can be observed that the connecting curve between the tunnels becomes thinner with a greater φ. The thinner connecting curve means a weaker interaction between the double tunnels. Then, the failure patterns transform to a single side-wall failure with the increase in φ. This trend illustrates that the stiffer (namely, the greater internal friction angle) the soil is, the weaker the interaction between the tunnels becomes.

6. Design Tables

Tables 1–4 present the predictions of seismic bearing capacity factor of double tunnels in cohesion–frictional soil from AFELA. For convenience, boldface numbers are employed to express the minimum critical interaction distance for each case. In addition, readers can identify the probable failure patterns by these boldface numbers. The failure patterns for cases above the boldface numbers are cross-shaped failures or half-cross-shaped failures. Additionally, the failure patterns for the remaining cases are all single sided-wall failures.

Table 1. Seismic bearing capacity N_{cs} with $k_h = 0.05$.

H/D	*S/D*	$\gamma D/c = 0$				$\gamma D/c = 1$			
		φ							
		5°	**10°**	**15°**	**20°**	**5°**	**10°**	**15°**	**20°**
1	1.5	1.76	2.04	2.43	2.97	0.52	0.75	1.06	1.51
	2	2.10	2.51	3.08	3.92	0.82	1.19	1.70	2.47
	2.5	2.46	3.02	3.81	5.05	1.12	1.63	2.39	3.56
	3	2.76	**3.44**	**4.46**	**6.12**	1.44	**2.13**	**3.08**	**4.40**
	3.5	**2.77**	3.44	4.46	6.12	**1.62**	2.13	3.08	4.40
	4	2.77	3.44	4.46	6.12	1.62	2.14	3.08	4.40
	4.5	2.77	3.44	4.46	6.12	1.62	2.13	3.08	4.40
	5	2.77	3.44	4.46	6.12	1.62	2.13	3.08	4.40
2	1.5	2.74	3.39	4.37	5.98	0.38	0.83	1.51	2.70
	2	2.90	3.60	4.65	6.33	0.52	1.06	1.88	3.26
	2.5	3.14	3.94	5.16	7.14	0.71	1.37	2.41	4.17
	3	3.34	4.24	5.65	8.04	0.95	1.74	2.99	5.15
	3.5	3.52	4.53	6.13	8.92	1.22	2.14	3.62	6.21
	4	3.80	4.96	6.87	10.23	1.39	2.45	4.06	7.40
	4.5	4.00	5.29	7.42	11.33	1.63	2.82	4.83	**8.59**
	5	4.24	5.68	8.10	12.67	1.79	**3.14**	**5.18**	8.59
	5.5	4.38	**5.91**	**8.40**	**12.96**	1.92	3.14	5.18	8.59
	6	**4.40**	5.91	8.40	12.96	**1.95**	3.14	5.18	8.59
	6.5	4.40	5.91	8.40	12.95	1.95	3.13	5.18	8.59
	7	4.40	5.91	8.40	12.96	1.95	3.14	5.18	8.59
	7.5	4.40	5.91	8.40	12.96	1.95	3.14	5.18	8.59
	8	4.40	5.91	8.40	12.96	1.95	3.14	5.18	8.59

Table 1. *Cont.*

H/D	*S/D*	$\gamma D/c = 0$				$\gamma D/c = 1$			
		φ							
		5°	**10°**	**15°**	**20°**	**5°**	**10°**	**15°**	**20°**
3	1.5	3.66	4.79	6.64	9.91	0.13	0.84	2.03	4.34
	2	3.68	4.78	6.57	9.82	0.15	0.89	2.18	4.62
	2.5	3.79	4.94	6.76	10.06	0.25	1.08	2.50	5.15
	3	3.93	5.12	7.06	10.54	0.42	1.37	2.97	5.94
	3.5	4.09	5.39	7.50	11.39	0.59	1.67	3.49	6.97
	4	4.26	5.67	8.03	12.39	0.76	1.97	4.23	8.02
	4.5	4.43	5.96	8.54	13.49	0.94	2.28	4.61	9.09
	5	4.62	6.27	9.10	14.55	1.12	2.59	5.18	10.28
	5.5	4.79	6.56	9.69	15.75	1.29	2.89	5.75	11.56
	6	4.96	6.86	10.22	17.07	1.46	3.19	6.28	12.65
	6.5	5.12	7.15	10.80	18.33	1.62	3.47	6.83	13.99
	7	5.29	7.43	11.38	19.62	1.78	3.58	6.94	**14.09**
	7.5	5.43	7.69	11.78	**19.84**	**1.86**	**3.53**	**6.97**	14.09
	8	5.47	7.72	**11.86**	19.83	1.86	3.55	6.97	14.09
	8.5	**5.49**	**7.73**	11.86	19.84	1.87	3.55	6.97	14.09
	9	5.49	7.73	11.86	19.84	1.87	3.55	6.97	14.09
	9.5	5.49	7.73	11.86	19.84	1.87	3.55	6.97	14.09
	10	5.49	7.73	11.86	19.84	1.87	3.55	6.97	14.09

Table 2. Seismic bearing capacity N_{cs} with $k_h = 0.1$.

H/D	*S/D*	$\gamma D/c = 0$				$\gamma D/c = 1$			
		φ							
		5°	**10°**	**15°**	**20°**	**5°**	**10°**	**15°**	**20°**
1	1.5	1.73	2.02	2.40	2.93	0.51	0.74	1.04	1.49
	2	2.07	2.47	3.03	3.86	0.81	1.16	1.67	2.43
	2.5	2.43	2.96	3.75	4.97	1.09	1.59	2.34	3.49
	3	2.71	3.21	4.18	5.97	1.39	2.03	2.99	3.97
	3.5	2.72	3.37	4.24	**6.07**	1.53	2.08	**3.04**	**4.28**
	4	2.73	**3.42**	**4.42**	6.07	1.57	**2.11**	3.04	4.28
	4.5	**2.75**	3.42	4.42	6.07	**1.60**	2.11	3.04	4.28
	5	2.75	3.43	4.43	6.07	1.60	2.11	3.03	4.28
2	1.5	2.70	3.34	4.30	5.88	0.37	0.80	1.48	2.65
	2	2.85	3.54	4.57	6.23	0.51	1.03	1.84	3.20
	2.5	3.07	3.87	5.06	7.02	0.69	1.34	2.36	4.09
	3	3.28	4.16	5.54	7.89	0.92	1.69	2.92	5.04
	3.5	3.46	4.45	6.04	8.74	1.18	2.08	3.54	6.07
	4	3.73	4.88	6.74	10.02	1.33	2.39	4.09	7.21
	4.5	3.92	5.19	7.29	11.16	1.59	2.74	4.69	8.36
	5	4.15	5.55	7.95	12.47	1.70	2.92	4.97	8.89
	5.5	4.21	5.65	8.11	12.60	1.80	3.00	5.05	**8.97**
	6	4.24	5.70	8.16	**12.80**	1.85	3.06	**5.08**	8.97
	6.5	4.28	5.77	**8.15**	12.80	1.89	3.07	5.08	8.97
	7	4.31	**5.78**	8.13	12.80	1.91	**3.08**	5.08	8.97
	7.5	**4.35**	5.78	8.15	12.79	**1.93**	3.08	5.08	8.97
	8	4.35	5.78	8.15	12.80	1.93	3.08	5.08	8.97

Table 2. *Cont.*

H/D	*S/D*	$\gamma D/c = 0$				$\gamma D/c = 1$			
		φ							
		5°	**10°**	**15°**	**20°**	**5°**	**10°**	**15°**	**20°**
3	1.5	3.59	4.70	6.49	9.70	0.12	0.82	1.99	4.20
	2	3.61	4.68	6.45	9.64	0.14	0.87	2.13	4.55
	2.5	3.72	4.83	6.64	9.88	0.23	1.06	2.44	5.07
	3	3.84	5.02	6.93	10.34	0.39	1.32	2.90	5.81
	3.5	4.00	5.28	7.36	11.19	0.55	1.60	3.42	6.80
	4	4.18	5.55	7.86	12.12	0.72	1.90	3.95	7.80
	4.5	4.34	5.84	8.36	13.22	0.89	2.20	4.47	8.98
	5	4.52	6.14	8.93	14.38	1.05	2.50	5.05	10.08
	5.5	4.69	6.42	9.49	15.51	1.21	2.78	5.58	11.23
	6	4.85	6.71	10.02	16.76	1.37	3.05	6.11	12.37
	6.5	5.00	6.98	10.57	17.97	1.52	3.26	6.38	13.18
	7	5.13	7.22	11.06	19.28	1.62	3.33	6.53	13.36
	7.5	5.18	7.30	11.28	19.55	1.67	3.40	6.63	**13.48**
	8	5.22	7.38	11.38	19.70	1.71	3.45	**6.70**	13.48
	8.5	5.25	7.42	11.44	19.73	1.74	3.46	6.70	13.48
	9	5.28	7.47	11.48	**19.76**	1.79	**3.48**	6.70	13.47
	9.5	5.30	7.51	**11.50**	19.76	1.80	3.48	6.70	13.48
	10	5.32	**7.54**	11.50	19.76	**1.81**	3.48	6.70	13.48
	10.5	**5.34**	7.54	11.51	19.76	1.81	3.48	6.71	13.48
	11	5.34	7.54	11.50	19.75	1.81	3.48	6.70	13.48
	11.5	5.34	7.54	11.51	19.76	1.81	3.48	6.70	13.48
	12	5.34	7.54	11.50	19.76	1.81	3.48	6.70	13.48

Table 3. Seismic bearing capacity N_{cs} with $k_h = 0.15$.

H/D	*S/D*	$\gamma D/c = 0$				$\gamma D/c = 1$			
		φ							
		5°	**10°**	**15°**	**20°**	**5°**	**10°**	**15°**	**20°**
1	1.5	1.70	1.98	2.35	2.88	0.50	0.72	1.02	1.46
	2	2.03	2.42	2.97	3.78	0.78	1.12	1.62	2.36
	2.5	2.38	2.91	3.67	4.88	1.05	1.54	2.26	3.39
	3	2.59	3.16	4.02	5.73	1.33	1.94	2.76	3.90
	3.5	2.64	3.31	4.08	**5.98**	1.45	1.98	**2.77**	**4.14**
	4	2.68	3.37	**4.36**	5.98	1.53	**2.08**	2.77	4.14
	4.5	**2.70**	**3.40**	4.36	5.98	**1.55**	2.08	2.77	4.14
	5	2.70	3.40	4.36	5.98	1.55	2.08	2.77	4.14
2	1.5	2.64	3.25	4.20	5.75	0.35	0.78	1.44	2.59
	2	2.78	3.45	4.45	6.09	0.48	0.99	1.79	3.10
	2.5	3.00	3.76	4.93	6.86	0.65	1.29	2.27	3.96
	3	3.19	4.06	5.41	7.69	0.87	1.62	2.82	4.91
	3.5	3.38	4.35	5.89	8.57	1.11	1.99	3.40	5.91
	4	3.63	4.75	6.57	9.83	1.25	2.27	3.96	7.00
	4.5	3.81	5.05	7.09	10.89	1.45	2.57	4.36	7.81
	5	3.94	5.25	7.51	11.79	1.56	2.67	4.58	8.23
	5.5	3.98	5.33	7.59	12.05	1.62	2.75	4.69	8.53
	6	4.01	5.39	7.72	12.18	1.67	2.82	4.78	**8.59**
	6.5	4.07	5.47	7.84	**12.25**	1.71	2.89	**4.83**	8.59
	7	4.10	5.51	7.90	12.25	1.75	2.93	4.82	8.59
	7.5	4.13	5.57	**7.99**	12.26	1.78	**2.95**	4.83	8.59
	8	4.15	**5.58**	7.99	12.25	1.81	2.95	4.82	8.58
	8.5	4.21	5.58	7.99	12.25	1.83	2.95	4.82	8.58
	9	**4.23**	5.58	7.99	12.25	**1.87**	2.95	4.82	8.59
	9.5	4.23	5.58	7.99	12.25	1.87	2.95	4.83	8.58
	10	4.24	5.58	7.99	12.25	1.87	2.95	4.82	8.58

Table 3. *Cont.*

H/D	*S/D*	$\gamma D/c = 0$				$\gamma D/c = 1$			
		φ							
		5°	**10°**	**15°**	**20°**	**5°**	**10°**	**15°**	**20°**
3	1.5	3.49	4.56	6.29	9.37	0.10	0.78	1.91	4.05
	2	3.51	4.56	6.28	9.38	0.10	0.82	2.06	4.39
	2.5	3.61	4.69	6.45	9.61	0.19	1.00	2.36	4.92
	3	3.73	4.87	6.73	10.09	0.34	1.25	2.78	5.62
	3.5	3.89	5.12	7.16	10.89	0.49	1.51	3.26	6.61
	4	4.06	5.39	7.63	11.88	0.64	1.80	3.79	7.57
	4.5	4.22	5.68	8.16	12.79	0.80	2.08	4.30	8.65
	5	4.39	5.97	8.72	13.98	0.95	2.35	4.83	9.75
	5.5	4.55	6.24	9.26	15.14	1.10	2.61	5.31	10.86
	6	4.70	6.52	9.76	16.29	1.23	2.83	5.69	11.96
	6.5	4.80	6.72	10.27	17.59	1.33	2.92	5.85	12.17
	7	4.84	6.79	10.38	17.98	1.39	2.99	5.94	12.43
	7.5	4.86	6.86	10.50	18.40	1.44	3.05	6.10	12.66
	8	4.90	6.93	10.64	18.56	1.47	3.13	6.19	12.94
	8.5	4.94	6.97	10.76	18.74	1.51	3.17	6.27	13.06
	9	4.97	7.02	10.84	18.80	1.55	3.22	6.35	13.13
	9.5	4.99	7.07	10.98	**18.88**	1.57	3.25	6.37	**13.22**
	10	5.02	7.11	11.00	18.88	1.60	3.30	6.36	13.22
	10.5	5.04	7.17	11.01	18.88	1.63	3.32	**6.42**	13.22
	11	5.06	7.18	11.09	18.88	1.65	3.33	6.42	13.22
	11.5	5.09	7.20	**10.94**	18.88	1.67	**3.35**	6.42	13.22
	12	5.10	**7.23**	10.93	18.88	1.68	3.36	6.42	13.22
	12.5	**5.11**	7.23	10.93	18.88	**1.69**	3.35	6.41	13.22
	13	5.11	7.23	10.93	18.88	1.69	3.35	6.42	13.22

Table 4. Seismic bearing capacity N_{cs} with $k_h = 0.2$.

H/D	*S/D*	$\gamma D/c = 0$				$\gamma D/c = 1$			
		φ							
		5°	**10°**	**15°**	**20°**	**5°**	**10°**	**15°**	**20°**
1	1.5	1.67	1.93	2.29	2.80	0.48	0.70	0.99	1.49
	2	1.99	2.37	2.90	3.68	0.74	1.09	1.57	2.29
	2.5	2.32	2.83	3.58	4.75	1.00	1.47	2.17	3.27
	3	2.50	2.88	3.95	5.36	1.25	1.78	2.67	3.79
	3.5	2.46	3.15	3.86	**5.65**	1.33	1.86	2.71	**3.97**
	4	2.64	3.18	4.05	5.65	**1.40**	**1.97**	**2.81**	3.97
	4.5	2.65	**3.22**	**4.14**	5.65	1.40	1.97	2.81	3.97
	5	**2.68**	3.22	4.14	5.65	1.40	1.97	2.81	3.97
2	1.5	2.55	3.16	4.07	5.55	0.32	0.74	1.38	2.48
	2	2.70	3.34	4.31	5.88	0.44	0.94	1.71	2.99
	2.5	2.91	3.65	4.77	6.64	0.60	1.21	2.18	3.80
	3	3.10	3.91	5.26	7.46	0.80	1.53	2.65	4.72
	3.5	3.27	4.21	5.71	8.31	1.03	1.88	3.24	5.67
	4	3.51	4.60	6.37	9.56	1.14	2.13	3.75	6.70
	4.5	3.60	4.76	6.70	10.35	1.31	2.31	3.95	7.10
	5	3.70	4.92	6.97	10.94	1.36	2.39	4.12	7.48
	5.5	3.73	4.97	7.06	11.06	1.41	2.46	4.25	7.71
	6	3.76	5.01	7.17	11.22	1.46	2.52	4.35	7.80
	6.5	3.80	5.08	7.30	11.44	1.48	2.59	4.43	8.10
	7	3.83	5.14	7.37	11.73	1.53	2.65	4.53	8.12
	7.5	3.87	5.20	7.47	11.91	1.56	2.70	4.61	**8.14**
	8	3.89	5.23	7.55	11.97	1.59	2.74	4.62	8.14
	8.5	3.90	5.25	7.52	12.01	1.63	2.76	**4.64**	8.14
	9	3.94	5.31	7.65	**12.00**	1.64	2.79	4.64	8.13
	9.5	3.96	5.35	**7.68**	12.00	1.67	**2.81**	4.64	8.14
	10	3.98	5.36	7.68	11.98	1.69	2.81	4.64	8.14
	10.5	3.99	**5.39**	7.68	12.00	**1.71**	2.81	4.64	8.14
	11	**4.00**	5.39	7.68	12.00	1.71	2.81	4.64	8.14
	11.5	4.00	5.39	7.68	12.00	1.71	2.81	4.64	8.13
	12	4.00	5.39	7.68	12.00	1.71	2.81	4.64	8.14
	12.5	4.00	5.39	7.68	12.00	1.71	2.81	4.64	8.14
	13	4.00	5.39	7.68	12.00	1.71	2.81	4.64	8.13

Table 4. *Cont.*

H/D	*S/D*	$\gamma D/c$ = 0				$\gamma D/c$ = 1			
		φ							
		5°	10°	15°	20°	5°	10°	15°	20°
	1.5	3.36	4.38	6.06	9.01	0.06	0.72	1.81	3.85
	2	3.38	4.39	6.04	9.03	0.07	0.76	1.95	4.21
	2.5	3.48	4.52	6.21	9.27	0.14	0.93	2.23	4.73
	3	3.60	4.71	6.49	9.53	0.28	1.16	2.64	5.44
	3.5	3.76	4.95	6.94	10.53	0.42	1.41	3.10	6.27
	4	3.92	5.22	7.39	11.41	0.55	1.67	3.60	7.26
	4.5	4.07	5.49	7.89	12.51	0.70	1.92	4.09	8.32
	5	4.23	5.75	8.40	13.56	0.82	2.16	4.55	9.35
	5.5	4.37	6.02	8.90	14.64	0.94	2.37	4.95	10.39
	6	4.42	6.16	9.33	15.82	1.02	2.47	5.10	10.82
	6.5	4.45	6.22	9.45	16.38	1.09	2.55	5.21	11.05
	7	4.48	6.28	9.57	16.71	1.13	2.61	5.31	11.24
	7.5	4.51	6.33	9.72	16.93	1.16	2.66	5.42	11.46
	8	4.54	6.37	9.80	17.08	1.20	2.70	5.52	11.74
	8.5	4.56	6.41	9.84	17.23	1.23	2.76	5.62	11.85
	9	4.58	6.46	9.96	17.49	1.25	2.81	5.69	12.00
	9.5	4.61	6.50	10.07	17.68	1.27	2.84	5.76	12.22
3	10	4.63	6.55	10.14	17.77	1.30	2.89	5.85	12.34
	10.5	4.65	6.60	10.23	18.03	1.33	2.94	5.92	12.48
	11	4.68	6.62	10.29	18.13	1.34	2.98	5.95	**12.51**
	11.5	4.69	6.67	10.38	18.25	1.37	3.01	6.04	12.51
	12	4.71	6.70	10.42	18.50	1.39	3.03	6.09	12.51
	12.5	4.72	6.75	10.49	**18.55**	1.41	3.08	**6.13**	12.51
	13	4.74	6.76	10.52	18.56	1.43	3.10	6.13	12.51
	14	4.76	6.78	10.57	18.55	1.51	**3.12**	6.13	12.51
	15	4.79	6.84	10.58	18.55	1.53	3.13	6.13	12.51
	16	4.80	6.85	**10.63**	18.55	**1.56**	3.13	6.13	12.51
	17	4.82	6.86	10.63	18.56	1.56	3.12	6.13	12.51
	18	4.83	6.88	10.63	18.55	1.56	3.13	6.13	12.51
	19	4.84	**6.91**	10.63	18.55	1.56	3.13	6.13	12.51
	20	4.85	6.91	10.63	18.55	1.56	3.12	6.13	12.51
	21	4.85	6.91	10.63	18.55	1.56	3.13	6.13	12.51
	22	**4.87**	6.91	10.63	18.55	1.56	3.13	6.13	12.51
	23	4.87	6.91	10.63	18.55	1.56	3.13	6.13	12.51
	24	4.87	6.91	10.63	18.55	1.56	3.12	6.13	12.51

7. Conclusions

This study employed self-developed AFELA code to investigate the effect of several influential factors on the seismic bearing of double unlined parallel tunnels in cohesion-frictional soil. Rigorous UB and LB results were obtained, which agree well with previous studies and the relative errors of which are less than 7%. The failure patterns and the scope of collapse with different influential factors are discussed. Additionally, detailed design tables were presented to facilitate the utilization of engineering practices. After investigations by AFELA code, several conclusions can be drawn as follows:

(1) The greater the $\gamma D/c$ is, the greater the seismic bearing capacity becomes. Additionally, the variations in $\gamma D/c$ and H/D linearly affect the seismic bearing capacity.

(2) The critical interaction distance between the double tunnels would be stronger with the increase in H/D and k_h and the decrease in φ, $\gamma D/c$. Additionally, the further the distance between the tunnels is, the weaker the interaction becomes.

(3) Three typical failure patterns can be summarized as follows: (a) single side-wall failure, which is the most stable condition, meaning that there is no interaction between the dual tunnels; (b) half-cross-shaped failure, meaning that there is a moderate interaction between the dual tunnels, and its stability is lower than the former one; and (c) cross-shaped failure, which means that there is an intense interaction between the dual tunnels, and the stability of this failure pattern is the worst.

(4) Before the failure pattern transforms to the single side-wall failure, the scope of collapse would be broader with the increase in S/D, H/D and k_h, while the strength of soil (φ and $\gamma D/c$) has almost no influence on the scope of collapse.

Author Contributions: Funding acquisition, G.W.; Investigation, Y.Z.; Software, Y.Z. and G.W.; Writing—original draft, G.W. All authors have read and agreed to the published version of the manuscript.

Funding: This research was funded by the National Natural Science Foundation of China (No. 51978255), the Shuimu Tsinghua Scholar Project of Tsinghua University (No. 2021SM007) and the Postgraduate Scientific Research Innovation Project of Hunan Province, China (No. CX20200394).

Data Availability Statement: The data presented in this study are available on request from the corresponding author.

Acknowledgments: The authors would like to acknowledge the financial support of the National Natural Science Foundation of China (No. 51978255), the Shuimu Tsinghua Scholar Project of Tsinghua University (No. 2021SM007) and the Postgraduate Scientific Research Innovation Project of Hunan Province, China (No. CX20200394).

Conflicts of Interest: The authors declare no conflict of interest.

References

1. Davis, E.H.; Gunn, M.J.; Mair, R.J.; Seneviratine, H.N. The stability of shallow tunnels and underground openings in cohesive material. *Géotechnique* **1980**, *30*, 397–416. [CrossRef]
2. Mühlhaus, H.B. Lower bound solutions for circular tunnels in two and three dimensions. *Rock Mech. Rock Eng.* **1985**, *18*, 37–52. [CrossRef]
3. Osman, A.S.; Mair, R.J.; Bolton, M.D. On the kinematics of 2D tunnel collapse in undrained clay. *Géotechnique* **2006**, *56*, 585–595. [CrossRef]
4. Leca, E.; Dormieux, L. Upper and lower bound solutions for the face stability of shallow circular tunnels in frictional material. *Géotechnique* **1990**, *40*, 581–606. [CrossRef]
5. Guang-Hui, C.; Jin-Feng, Z.; Qi, M.; Wu-Jun, G.; Tai-Zhong, Z. Face stability analysis of a shallow square tunnel in non-homogeneous soils. *Comput. Geotech.* **2019**, *114*, 103112. [CrossRef]
6. Wu, G.; Zhao, H.; Zhao, M.; Zhu, Z. Stochastic analysis of dual tunnels in spatially random soil. *Comput. Geotech.* **2021**, *129*, 103861. [CrossRef]
7. Sahoo, J.P.; Kumar, J. Seismic stability of a long unsupported circular tunnel. *Comput. Geotech.* **2012**, *44*, 109–115. [CrossRef]
8. Wu, G.; Zhao, M.; Zhang, R.; Liang, G. Ultimate bearing capacity of eccentrically loaded strip footings above voids in rock masses. *Comput. Geotech.* **2020**, *128*, 103819. [CrossRef]
9. Wu, G.; Zhao, M.; Zhao, H.; Xiao, Y. Effect of Eccentric Load on the Undrained Bearing Capacity of Strip Footings above Voids. *Int. J. Geomech.* **2020**, *20*, 04020078. [CrossRef]
10. Mohammad, R.K.; Ali, Z. Fracture and load-carrying capacity of 3D-printed cracked components. *Extrem. Mech. Lett.* **2020**, *37*, 100692.
11. Rebecca, W.; Fernando, C.; Jochen, H. High resolution modeling of the impact of urbanization and green infrastructure on the water and energy balance. *Urban Clim.* **2021**, *39*, 100961.
12. Chakraborty, D.; Kumar, J. Stability of a long unsupported circular tunnel in soils with seismic forces. *Nat. Hazards* **2013**, *68*, 419–431. [CrossRef]
13. Zhang, P.; Wu, H.-N.; Chen, R.-P.; Chan, T.H. Hybrid meta-heuristic and machine learning algorithms for tunneling-induced settlement prediction: A comparative study. *Tunn. Undergr. Space Technol.* **2020**, *99*, 103383. [CrossRef]
14. Zhang, P.; Chen, R.-P.; Wu, H.-N. Real-time analysis and regulation of EPB shield steering using Random Forest. *Autom. Constr.* **2019**, *106*, 102860. [CrossRef]
15. Ukritchon, B.; Yoang, S.; Keawsawasvong, S. Undrained stability of unsupported rectangular excavations in non-homogeneous clays. *Comput. Geotech.* **2019**, *117*, 103281. [CrossRef]
16. Sahoo, J.P.; Kumar, J. Stability of a circular tunnel in presence of pseudostatic seismic body forces. *Tunn. Undergr. Space Technol.* **2014**, *42*, 264–276. [CrossRef]
17. Soliman, E.; Duddeck, H.; Ahrens, H. Two- and three-dimensional analysis of closely spaced double-tube tunnels. *Tunn. Undergr. Space Technol.* **1993**, *8*, 13–18. [CrossRef]
18. Kim, S.H.; Burd, H.J.; Milligan, G.W.E. Model testing of closely spaced tunnels in clay. *Géotechnique* **1998**, *48*, 375–388. [CrossRef]
19. Lanzano, G.; Bilotta, E.; Russo, G.; Silvestri, F.; Madabhushi, S.P.G. Centrifuge Modeling of Seismic Loading on Tunnels in Sand. *Geotech. Test. J.* **2012**, *35*, 854–869. [CrossRef]
20. Abate, G.; Massimino, M.R.; Maugeri, M. Numerical modelling of centrifuge tests on tunnel–soil systems. *Bull. Earthq. Eng.* **2014**, *13*, 1927–1951. [CrossRef]
21. Osman, A.S. Stability of unlined twin tunnels in undrained clay. *Tunn. Undergr. Space Technol.* **2010**, *25*, 290–296. [CrossRef]

22. Sahoo, J.P.; Kumar, J. Stability of long unsupported twin circular tunnels in soils. *Tunn. Undergr. Space Technol.* **2013**, *38*, 326–335. [CrossRef]
23. Sahoo, J.P.; Kumar, J. Required Lining Pressure for the Stability of Twin Circular Tunnels in Soils. *Int. J. Géoméch.* **2018**, *18*, 04018069. [CrossRef]
24. Yamamoto, K.; Lyamin, A.; Wilson, D.W.; Sloan, S.; Abbo, A.J. Stability of dual square tunnels in cohesive-frictional soil subjected to surcharge loading. *Can. Geotech. J.* **2014**, *51*, 829–843. [CrossRef]
25. Zhang, J.; Yang, F.; Yang, J.; Zheng, X.; Zeng, F. Upper-bound stability analysis of dual unlined elliptical tunnels in cohesive-frictional soils. *Comput. Geotech.* **2016**, *80*, 283–289. [CrossRef]
26. Zhang, J.; Feng, T.; Yang, J.; Yang, F.; Gao, Y. Upper-bound stability analysis of dual unlined horseshoe-shaped tunnels subjected to gravity. *Comput. Geotech.* **2018**, *97*, 103–110. [CrossRef]
27. Yang, F.; Sun, X.; Zheng, X.; Yang, J. Stability analysis of a deep buried elliptical tunnel in cohesive–frictional (c–ϕ) soil with a nonassociated flow rule. *Can. Geotech. J.* **2016**, *54*, 736–741. [CrossRef]
28. Yang, F.; Zheng, X.; Zhang, J.; Yang, J. Upper bound analysis of stability of dual circular tunnels subjected to surcharge loading in cohesive-frictional soils. *Tunn. Undergr. Space Technol.* **2017**, *61*, 150–160. [CrossRef]
29. Xiao, Y.; Zhao, M.; Zhang, R.; Zhao, H.; Peng, W. Stability of two circular tunnels at different depths in cohesive-frictional soils subjected to surcharge loading. *Comput. Geotech.* **2019**, *112*, 23–34. [CrossRef]
30. Vahid, M.; Alireza, M. Seismic reliability evaluation of tunnel form (box-type) RC structures under the accidental torsion. *Struct. Concr.* **2018**, *19*, 1927–1938.
31. Mohsenian, V.; Hajirasouliha, I.; Mariani, S.; Nikkhoo, A. Seismic reliability assessment of RC tunnel-form structures with geometric irregularities using a combined system approach. *Soil Dyn. Earthq. Eng.* **2020**, *139*, 106356. [CrossRef]
32. Yue, F.; Liu, B.; Zhu, B.; Jiang, X.; Chen, S.; Jaisee, S.; Chen, L.; Lv, B. Shaking table investigations on seismic performance of prefabricated corrugated steel utility tunnels. *Tunn. Undergr. Space Technol.* **2020**, *105*, 103579. [CrossRef]
33. Thomasz, M.; Damian, B.; Joanna, N. Seismic vulnerability of a soil-steel composite tunnel—Norway Tolpinrud Railway Tunnel Case Study. *Tunn. Undergr. Space Technol.* **2021**, *110*, 103808.
34. Merifield, R.S.; Sloan, S.W.; Yu, H.S. Stability of plate anchors in undrained clay. *Géotechnique* **2001**, *51*, 141–153. [CrossRef]
35. Sloan, S. Geotechnical stability analysis. *Géotechnique* **2013**, *63*, 531–571. [CrossRef]
36. Krabbenhoft, K.; Lyamin, A.V.; Hjiaj, M.; Sloan, S.W. A new discontinuous upper bound limit analysis formulation. *Int. J. Numer. Methods Eng.* **2005**, *63*, 1069–1088. [CrossRef]
37. Lyamin, A.V.; Krabbenhoft, K.; Abbo, A.J. General approach to modelling discontinuities in limit analysis. In Proceedings of the 11th International Conference International Association Computer Methods and Advances in Geomechanics (IACMAG 2005), Torino, Italy, 19–24 June 2005; Volume 1, pp. 95–102.
38. Ciria, H.; Peraire, J.; Bonet, J. Mesh adaptive computation of upper and lower bounds in limit analysis. *Int. J. Numer. Methods Eng.* **2008**, *75*, 899–944. [CrossRef]
39. Muñoz, J.J.; Bonet, J.; Huerta, A.; Peraire, J. Upper and lower bounds in limit analysis: Adaptive meshing strategies and discontinuous loading. *Int. J. Numer. Methods Eng.* **2009**, *77*, 471–501. [CrossRef]
40. Herskovits, J.; Mappa, P.; Goulart, E.; Soares, C.M. Mathematical programming models and algorithms for engineering design optimization. *Comput. Methods Appl. Mech. Eng.* **2005**, *194*, 3244–3268. [CrossRef]
41. Zhang, R.; Li, L.; Zhao, L.; Tang, G. An adaptive remeshing procedure for discontinuous finite element limit analysis. *Int. J. Numer. Methods Eng.* **2018**, *116*, 287–307. [CrossRef]
42. Krabbenhoft, K.; Lyamin, A.; Krabbenhoft, J. Optum Computational Engineering (OptumG2). 2015. Available online: www.optumce.com (accessed on 2 September 2021).